

Proper motion, spectra, and timing of PSR J1813–1749 using *Chandra* and *NICER*

Wynn C. G. Ho¹*, Sebastien Guillot^{2,3}, P.M. Saz Parkinson^{4,5}, B. Limyansky⁵, C.-Y. Ng⁶, Michał Bejger⁷, Cristóbal M. Espinoza⁸, B. Haskell⁷, Gaurava K. Jaisawal⁹, and C. Malacaria^{10,11†}

¹Department of Physics and Astronomy, Haverford College, 370 Lancaster Avenue, Haverford, PA, 19041, USA

²IRAP, CNRS, 9 avenue du Colonel Roche, BP 44346, F-31028 Toulouse Cedex 4, France

³Université de Toulouse, CNES, UPS-OMP, F-31028 Toulouse, France

⁴Department of Physics and Laboratory for Space Research, The University of Hong Kong, Pokfulam Road, Hong Kong

⁵Santa Cruz Institute for Particle Physics, University of California, Santa Cruz, CA, 95064, USA

⁶Department of Physics, The University of Hong Kong, Pokfulam Road, Hong Kong

⁷Nicolaus Copernicus Astronomical Center, Polish Academy of Sciences, ul. Bartycka 18, 00-716 Warsaw, Poland

⁸Departamento de Física, Universidad de Santiago de Chile, Avenida Ecuador 3493, 9170124 Estación Central, Santiago, Chile

⁹National Space Institute, Technical University of Denmark, Elektrovej 327-328, DK-2800 Lyngby, Denmark

¹⁰NASA Marshall Space Flight Center, NSSTC, 320 Sparkman Drive, Huntsville, AL 35805, USA

¹¹Universities Space Research Association, Science and Technology Institute, 320 Sparkman Drive, Huntsville, AL 35805, USA

Accepted 2020 August 27. Received 2020 August 26; in original form 2020 July 2

ABSTRACT

PSR J1813–1749 is one of the most energetic rotation-powered pulsars known, producing a pulsar wind nebula (PWN) and gamma-ray and TeV emission, but whose spin period is only measurable in X-ray. We present analysis of two *Chandra* datasets that are separated by more than ten years and recent *NICER* data. The long baseline of the *Chandra* data allows us to derive a pulsar proper motion $\mu_{\text{R.A.}} = -(0''.067 \pm 0''.010) \text{ yr}^{-1}$ and $\mu_{\text{decl.}} = -(0''.014 \pm 0''.007) \text{ yr}^{-1}$ and velocity $v_{\perp} \approx 900 - 1600 \text{ km s}^{-1}$ (assuming a distance $d = 3 - 5 \text{ kpc}$), although we cannot exclude a contribution to the change in measured pulsar position due to a change in brightness structure of the PWN very near the pulsar. We model the PWN and pulsar spectra using an absorbed power law and obtain best-fit absorption $N_{\text{H}} = (13.1 \pm 0.9) \times 10^{22} \text{ cm}^{-2}$, photon index $\Gamma = 1.5 \pm 0.1$, and 0.3–10 keV luminosity $L_{\text{X}} \approx 5.4 \times 10^{34} \text{ erg s}^{-1} (d/5 \text{ kpc})^2$ for the PWN and $\Gamma = 1.2 \pm 0.1$ and $L_{\text{X}} \approx 9.3 \times 10^{33} \text{ erg s}^{-1} (d/5 \text{ kpc})^2$ for PSR J1813–1749. These values do not change between the 2006 and 2016 observations. We use *NICER* observations from 2019 to obtain a timing model of PSR J1813–1749, with spin frequency $\nu = 22.35 \text{ Hz}$ and spin frequency time derivative $\dot{\nu} = (-6.428 \pm 0.003) \times 10^{-11} \text{ Hz s}^{-1}$. We also fit ν measurements from 2009–2012 and our 2019 value and find a long-term spin-down rate $\dot{\nu} = (-6.3445 \pm 0.0004) \times 10^{-11} \text{ Hz s}^{-1}$. We speculate that the difference in spin-down rates is due to glitch activity or emission mode switching.

Key words: ISM: individual: G12.82–0.02, HESS J1813–178 – ISM: supernova remnants – pulsars: general – pulsars: individual: CXOU J181335.16–174957.4, PSR J1813–1749 – X-rays: stars

1 INTRODUCTION

PSR J1813–1749 (also known as CXOU J181335.16–174957.4) has a previously measured spin frequency $\nu = 22.37 \text{ Hz}$ and spin-rate change

$\dot{\nu} = -6.333 \times 10^{-11} \text{ Hz s}^{-1}$ (Gotthelf & Halpern 2009; Halpern et al. 2012), which make this pulsar’s spin-down energy loss rate $\dot{E} = 5.6 \times 10^{37} \text{ erg s}^{-1}$ the fourth largest among the 2800 known pulsars, behind only PSR J0537–6910, the Crab pulsar, and PSR B0540–69 (Manchester et al. 2005). This large rate probably explains the pulsar’s association with the TeV source HESS J1813–178 (Ubertini et al. 2005) and gamma-ray source IGR J18135–1751

* E-mail: wynnho@slac.stanford.edu
† NASA Postdoctoral Fellow

(Aharonian et al. 2005) and makes the pulsar an interesting target for LIGO/Virgo searches of continuous gravitational waves (Abbott et al. 2017, 2019a). The spin frequency is only measurable at X-ray energies, as it seems to be a variable, but unpulsed, radio source (Dzib et al. 2010, 2018). PSR J1813–1749 is located in the young (< 3 kyr) supernova remnant G12.82–0.02 (Brogan et al. 2005) at a distance $d \approx 3 - 5$ kpc (Messineo et al. 2011).

Observations at X-ray energies are crucial to the study of PSR J1813–1749. For example, the exceptional spatial resolving power of *Chandra* allows an accurate measurement of the position of PSR J1813–1749 and separation of the X-ray spectra of the pulsar and pulsar wind nebula (PWN) in which the pulsar is embedded. Using a 30 ks ACIS-I observation taken in 2006, Helfand et al. (2007) measure the pulsar position to be R.A. = $18^{\text{h}}13^{\text{m}}35\rlap{.}^{\text{s}}166$, decl. = $-17^{\circ}49'57\rlap{.}''48$ (J2000). They perform a spectral analysis on three spatial components, i.e., the PWN, an inner nebula, and the pulsar, and find each is well fit by an absorbed power law. More recently, Townsley et al. (2018) analyse a number of *Chandra* observations, including those considered here, to compile a catalog of X-ray sources and their spectral properties, such as those of PSR J1813–1749. Meanwhile, Halpern et al. (2012) use *Chandra* ACIS-S3 (in continuous clocking mode) and *XMM-Newton* EPIC-pn observations to measure the pulsar spin frequency at three epochs, in 2009, 2011, and 2012. While a simple linear fit of these measurements results in a value of $\dot{\nu}$, the three observations spanning three years are insufficient to obtain a rotation phase-connected timing model of PSR J1813–1749.

Here we re-analyse the 2006 *Chandra* observation and compare it to a set of 2016 observations. This comparison allows us to determine not only any long-term variability but also the pulsar proper motion over the ten-year timespan. We present detection of the spin frequency of PSR J1813–1749 using recent *NICER* data, which enables us to update the timing model that is vital for the most sensitive searches of continuous gravitational waves from this pulsar. In Section 2, we describe our analysis procedure for the *Chandra* data and present results on proper motion of PSR J1813–1749 and spectral modeling of the pulsar and PWN. In Section 3, we describe our pulsation search using *NICER* data and timing analysis of PSR J1813–1749. We summarize in Section 4.

2 ANALYSIS OF *Chandra* DATA

Chandra observed PSR J1813–1749 with ACIS-I for 30 ks on 2006 September 15 (ObsID 6685), for 13 ks on 2016 May 29 (ObsID 17695), and for 17 ks on 2016 June 5 (ObsID 17440); see Table 1. We reprocess data with `chandra_repro` and Chandra Interactive Analysis of Observations (CIAO) 4.11 and Calibration Database (CALDB) 4.8.5 (Fruscione et al. 2006). As in Helfand et al. (2007), we do not account for photon pile-up since, as they note, the maximum count rate centered on PSR J1813–1749 is $< 0.004 \text{ c s}^{-1}$ for ObsID 6685 and is $< 0.002 \text{ c s}^{-1}$ for ObsIDs 17440 and 17695. We note that Townsley et al. (2018) include a pile-up correction in their analysis of ObsID 6685 but not of 17440 and 17695.

Table 1. *Chandra* and *NICER* observations of PSR J1813–1749.

Telescope	ObsID	Date	Exposure (ks)
<i>Chandra</i>	6685	2006 September 15	30
<i>Chandra</i>	17695	2016 May 29	13
<i>Chandra</i>	17440	2016 June 5	17
<i>NICER</i>	1020440101	2018 August 25	6
<i>NICER</i>	2579030101	2019 June 28	17
<i>NICER</i>	2579030102	2019 June 29	22
<i>NICER</i>	2579030103	2019 June 30	13
<i>NICER</i>	2579030201	2019 July 10	3
<i>NICER</i>	2579030202	2019 July 11	7
<i>NICER</i>	2579030203	2019 July 12	17
<i>NICER</i>	2579030204	2019 July 13	23
<i>NICER</i>	2579030301	2019 July 30	5
<i>NICER</i>	2579030302	2019 July 31	18
<i>NICER</i>	2579030303	2019 August 1	13
<i>NICER</i>	2579030304	2019 August 2	6
<i>NICER</i>	2579030305	2019 August 3	1
<i>NICER</i>	2579030306	2019 August 4	6

2.1 Proper motion and velocity

We follow the recommended procedure¹ to improve *Chandra*'s astrometry. In particular, we use `wavdetect` to detect sources in each observation and `wcs_match` and `wcs_update` to match detected sources in each 2016 observation with those detected in the 2006 observation; ObsID 6685 is used as the reference dataset given its longer exposure time. We then run `wavdetect` on the updated datasets of ObsID 17695 and 17440 to obtain updated pulsar positions. The positions and 1σ uncertainties of PSR J1813–1749 are given in Table 2. Note that the position uncertainties determined by `wavdetect` suggest there could be a small increase (< 15 percent) in asymmetry in R.A. between 2006 and 2016, perhaps due to a brightness change in the PWN, although the PWN flux contribution near the pulsar is likely to be small. We also note that the position in ObsID 6685 is $0.''43$ from the position found by Helfand et al. (2007) (see Section 1) but is still consistent, given their 1σ uncertainty of $0.''3$. While we consider the absolute position (calibrated to optical sources in the USNO-B catalog) from Helfand et al. (2007) to be reliable, we use our measured position from ObsID 6685 for consistency in order to determine relative displacements and extract the pulsar spectrum.

From Table 2, we see that the position of PSR J1813–1749 after astrometric correction appears to be displaced to the southwest by $\approx 0.''7$ between 2006 and 2016. To refine this displacement, we select four of the nearest (to the pulsar) and brightest sources and use their position and 1σ uncertainty in each dataset as determined by `wavdetect`. These sources are shown in Figure 1 and their positions are given in Table 2; source names and labels are from Helfand et al. (2007); Townsley et al. (2018). There are a few other sources that are brighter (in ObsID 6685) than some of the four, but these other sources are fainter than the four chosen here in ObsID 17695 and/or 17440. We calculate a weighted (by square of uncertainty) mean shift of these four sources: $(\Delta\text{R.A.}, \Delta\text{decl.}) = (-0.''22 \pm 0.''07, -0.''16 \pm 0.''07)$ for ObsID 17695 and $(+0.''19 \pm 0.''08, -0.''20 \pm 0.''06)$ for ObsID

¹ https://cxc.harvard.edu/ciao/threads/reproject_aspect/

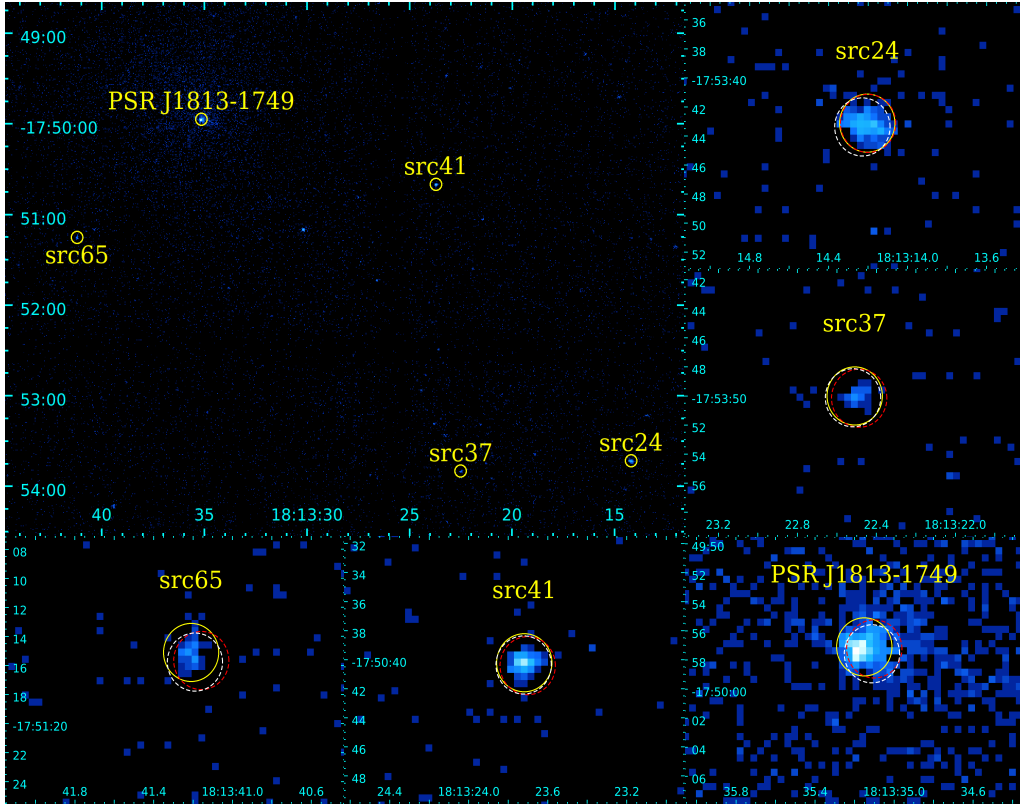


Figure 1. *Chandra* 2006 image (ObsID 6685) of PSR J1813–1749 and four nearby and bright sources that are used to refine the astrometry between 2006 and 2016. The latter four sources are labeled by their source number from Table 1 of Helfand et al. (2007) (see also Table 2). Solid yellow, dashed red, and dashed white circles (with radius of 2'' in all zoomed-in panels) indicate positions of each source in 2006, 2016 (ObsID 17695), and 2016 (ObsID 17440), respectively.

Table 2. Positions of X-ray sources. Source names are those from Townsley et al. (2018), while src# refers to the source number in Table 1 of Helfand et al. (2007). Number in parentheses is 1σ error in last digit.

ObsID	R.A.	decl.	Δ R.A.	Δ decl.
CXOU J181335.16–174957.4 (PSR J1813–1749)				
6685	18:13:35.151(2)	−17:49:57.10(3)		
17695	18:13:35.100(6)	−17:49:57.24(8)	−0''.73(10)	−0''.14(10)
17440	18:13:35.112(6)	−17:49:57.57(7)	−0''.55(10)	−0''.47(8)
CXOU J181314.20–175343.4 (src24)				
6685	18:13:14.204(4)	−17:53:43.12(5)		
17695	18:13:14.200(6)	−17:53:43.13(12)	−0''.05(11)	−0''.01(13)
17440	18:13:14.229(6)	−17:53:43.37(8)	+0''.36(11)	−0''.25(9)
CXOU J181322.48–175350.2 (src37)				
6685	18:13:22.510(13)	−17:53:50.00(7)		
17695	18:13:22.487(5)	−17:53:50.16(11)	−0''.33(20)	−0''.16(13)
17440	18:13:22.518(5)	−17:53:50.13(6)	+0''.11(20)	−0''.13(9)
CXOU J181323.71–175040.5 (src41)				
6685	18:13:23.719(3)	−17:50:40.21(3)		
17695	18:13:23.701(6)	−17:50:40.41(15)	−0''.26(10)	−0''.20(15)
17440	18:13:23.722(9)	−17:50:40.36(13)	+0''.04(13)	−0''.15(13)
CXOU J181341.20–175115.4 (src65)				
6685	18:13:41.210(8)	−17:51:15.11(17)		
17695	18:13:41.158(16)	−17:51:15.66(19)	−0''.74(25)	−0''.55(25)
17440	18:13:41.190(26)	−17:51:15.77(30)	−0''.28(38)	−0''.66(34)

17440. Accounting for this shift, we obtain a weighted mean displacement (Δ R.A., Δ decl.) = ($−0''.62 \pm 0''.09$, $−0''.15 \pm 0''.08$) for PSR J1813–1749. Considering the 9.7 year time difference between 2006 and 2016 observations, we determine that PSR J1813–1749 appears to be moving with a proper motion of $\mu_{\text{R.A.}} = (−0''.067 \pm 0''.010) \text{ yr}^{-1}$ and $\mu_{\text{decl.}} = (−0''.014 \pm 0''.007) \text{ yr}^{-1}$, after accounting for $\cos(\text{decl.})$ in the apparent R.A. motion of $(−0''.064 \pm 0''.009) \text{ yr}^{-1}$. For an uncertain distance of $\approx 3 - 5$ kpc (Messineo et al. 2011; Halpern et al. 2012), the proper motion implies a transverse velocity $v_{\perp} \approx 900 - 1600 \text{ km s}^{-1}$, with an uncertainty of $\sim 300 \text{ km s}^{-1}$. This velocity is high but not extraordinary compared to that measured for other neutron stars (Kargaltsev et al. 2017; Deller et al. 2019; Dang et al. 2020). Finally, the pulsar is $\sim 20''$ from the center of the supernova remnant G12.82–0.02 (see, e.g., Dzib et al. 2018), and therefore this velocity would indicate a pulsar age of ~ 300 yr, which is at the lower end of the age range of 200–3000 yr for the remnant (Brogan et al. 2005).

2.2 Spectra

Spectra are extracted using `specextract` from regions shown in Figure 2 (from ObsID 17440; see also Figure 13 of Kuiper & Hermen 2015 for an image from ObsID 6685) for the PWN, inner nebula, and pulsar. These regions are chosen to be the same as those used by Helfand et al. (2007)

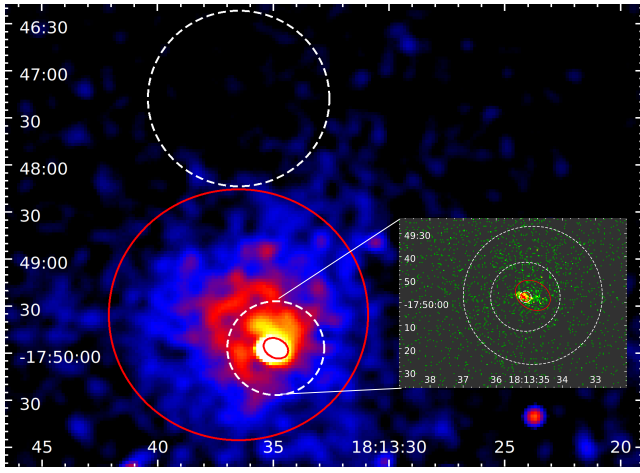


Figure 2. *Chandra* image (ObsID 17440) of the PWN, inner nebula, and PSR J1813–1749; 0.5–7 keV image is smoothed to make the PWN more visible. Inset: Zoomed-in unsmoothed view of inner nebula and PSR J1813–1749. Solid curves indicate extraction regions for the PWN (80'' radius), inner nebula (6'' × 8'' radii ellipse), and pulsar (2'' radius) spectra. Dotted curves indicate background extraction regions for the PWN (56'' radius), inner nebula (30'' radius), and pulsar (2''.5–15'' radii annulus). Embedded regions are excluded from each source's spectral extraction (see text for details).

and are different from that used in Townsley et al. (2018) for the pulsar. Specifically, source counts for the PWN are from a 80'' radius circle centered on R.A.= 18^h13^m36^s.50, decl.= −17°49'35''.6 and excluding the inner nebula source region, while background for the PWN is from a 56'' radius circle centered on R.A.= 18^h13^m36^s.50, decl.= −17°47'17''.6, i.e., 2.3° north of source region. Source counts for the inner nebula are from a 6'' × 8'' radii ellipse centered on R.A.= 18^h13^m34.89, decl.= −17°49'56''.9 and excluding the pulsar source region, while background for the inner nebula is from a 30'' radius circle centered on it and excluding the inner nebula region. Source counts for the pulsar are from a 2'' radius circle (which encircles an energy fraction of 90 percent at 4.5 keV) centered on its position as given in Table 2, while background for the pulsar is from a 2''.5–15'' radius circular annulus around the pulsar. Since ObsIDs 17440 and 17695 are taken only one week apart, we merge spectra extracted from these two observations using `combine_spectra` and `dmggroup`. PWN, inner nebula, and pulsar spectra are binned with a minimum of 30, 15, and 20 counts per energy bin, respectively. Fit results for the PWN and pulsar are the same within uncertainties when using a minimum of 15 counts per bin, as done in Helfand et al. (2007).

We perform spectral fitting using Xspec 12.10.1 (Arnaud 1996). We use an absorbed power law (PL) model composed of `tbabs` and `powerlaw`. The former is to model photoelectric absorption in the interstellar medium, with abundances from Wilms et al. (2000) and cross-sections from Verner et al. (1996); note that use of `phabs`, instead of `tbabs`, leads to very similar results except for a slightly higher best-fit N_{H} (= $13.4 \times 10^{22} \text{ cm}^{-2}$ for the PWN). The power law is to model the intrinsic spectrum of the pulsar or pulsar wind. For each set of spectra (PWN, inner nebula, and pul-

Table 3. Spectral fits with absorbed power law. Absorption N_{H} is in 10^{22} cm^{-2} , power law normalization is in $10^{-4} \text{ photon cm}^{-2} \text{ s}^{-1} \text{ keV}^{-1}$, and absorbed 2–10 keV flux f_{2-10}^{abs} is in $10^{-12} \text{ erg cm}^{-2} \text{ s}^{-1}$. Errors are 1σ , and parameter values without errors are fixed.

Year	N_{H}	Γ	PL norm.	f_{2-10}^{abs}	χ^2/dof
PWN					
2006	$13.11^{+0.89}_{-0.86}$	1.46 ± 0.12	$20.3^{+4.9}_{-3.9}$	$7.5^{+0.1}_{-0.3}$	330/308
2016			$20.7^{+5.0}_{-3.9}$	$7.7^{+0.1}_{-0.3}$	
2006	$12.6^{+1.3}_{-1.3}$	$1.32^{+0.17}_{-0.18}$	$16.0^{+5.6}_{-4.0}$	$7.8^{+0.1}_{-0.6}$	173/160
2016	$13.8^{+1.3}_{-1.2}$	$1.63^{+0.10}_{-0.17}$	$27.1^{+10.0}_{-7.1}$	$7.4^{+0.1}_{-0.9}$	153/146
inner nebula					
2006	13.1	0.77 ± 0.17	$0.40^{+0.12}_{-0.10}$	$0.54^{+0.04}_{-0.07}$	56.0/54
2016			$0.93^{+0.29}_{-0.22}$	1.2 ± 0.1	
2006	$14.9^{+9.2}_{-8.8}$	$0.47^{+0.84}_{-0.76}$	$0.27^{+1.1}_{-0.27}$	$\lesssim 0.6$	19.4/18
2016	$13.8^{+4.8}_{-4.4}$	$1.03^{+0.49}_{-0.46}$	$1.4^{+2.7}_{-0.8}$	$1.2^{+0.1}_{-1.0}$	33.5/33
PSR J1813–1749					
2006	13.1	1.24 ± 0.11	$2.79^{+0.49}_{-0.42}$	1.6 ± 0.1	55.8/66
2016			$2.77^{+0.50}_{-0.43}$	1.5 ± 0.1	
2006	$16.5^{+3.9}_{-3.6}$	$1.44^{+0.44}_{-0.42}$	$4.3^{+5.4}_{-2.3}$	$1.6^{+0.1}_{-0.7}$	34.7/37
2016	$14.7^{+4.1}_{-3.8}$	$1.67^{+0.50}_{-0.46}$	$5.6^{+9.2}_{-3.6}$	$1.4^{+0.1}_{-0.9}$	16.1/26

star), we conduct two different fits. For the PWN, we first allow varying but linked values of absorption and photon index between the 2006 and 2016 data, so that only the power law normalization varies between these two epochs. For the inner nebula and pulsar, our first fit fixes the absorption to the best-fit value of the PWN spectral model, i.e., $N_{\mathrm{H}} = 13.1 \times 10^{22} \text{ cm}^{-2}$ (see Table 3), but allows a varying but linked value of the photon index. The second fits have all model parameters free to vary and untied between observations.

The results of our different spectral fits are given in Table 3. A comparison between the fit where all PWN parameters are free to vary and the fit where some PWN parameters are tied between observations yields a *F*-test probability of 22 percent for the fit improvement of the former to be produced by chance. *F*-test comparisons for fits to the inner nebula and pulsar spectra yield probabilities of 41 percent and 11 percent, respectively. These probabilities indicate that tied values of N_{H} and photon index Γ are sufficient to describe the combined spectra, and we also see that all model parameter values for both sets of fits are within each other's uncertainties. Thus N_{H} and Γ do not change between 2006 and 2016 observations. While the PWN and pulsar fluxes are also the same, the inner nebula flux may be different, although uncertainties in the precise spectral extraction and inferred values allow for consistency between 2006 and 2016.

Figure 3 shows the PWN, inner nebula, and pulsar spectra and best-fit models, with model parameters tied between observations. For the PWN, $N_{\mathrm{H}} = (13.1 \pm 0.9) \times 10^{22} \text{ cm}^{-2}$, $\Gamma = 1.5 \pm 0.1$, and absorbed 2–10 keV flux $f_{2-10}^{\mathrm{abs}} \approx 7.6 \times 10^{-12} \text{ erg cm}^{-2} \text{ s}^{-1}$. The flux is constant across the 10 years between observations and equates to an unabsorbed 0.3–10 keV flux $f_X = 1.8 \times 10^{-11} \text{ erg cm}^{-2} \text{ s}^{-1}$ and luminosity

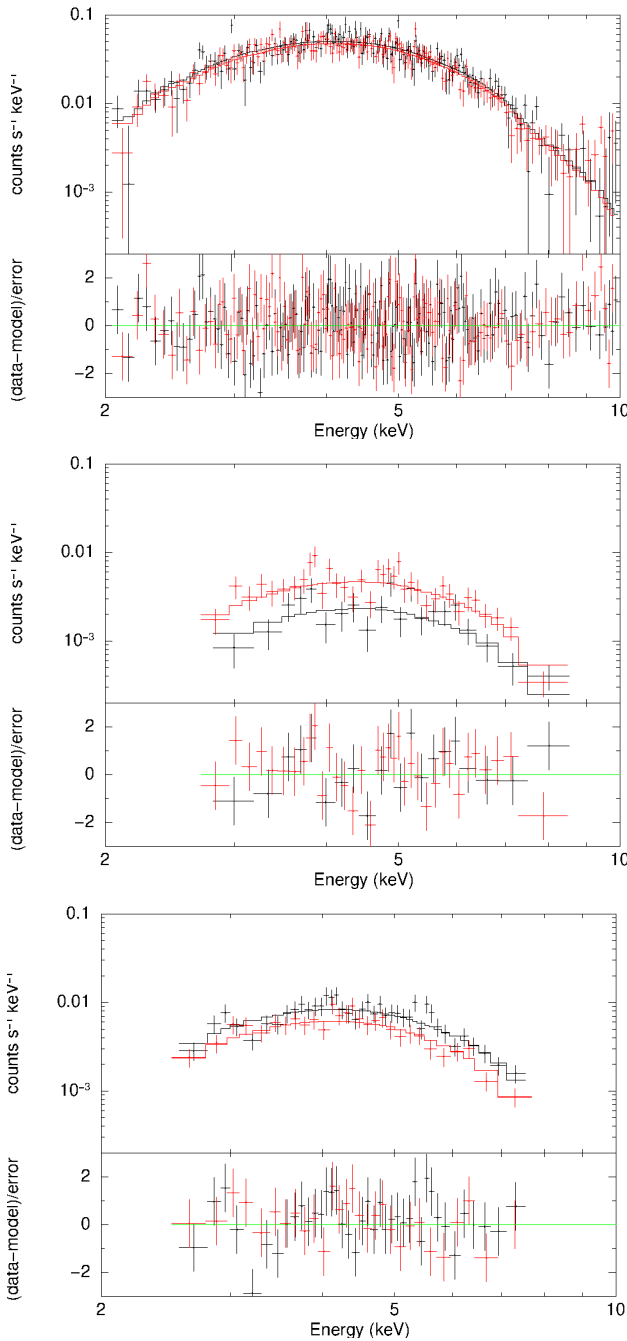


Figure 3. Upper panels show *Chandra* spectra (black for ObsID 6685 and red for merged 17695/17440) of the PWN (top), inner nebula (middle), and PSR J1813–1749 (bottom) and best-fit absorbed power law model. The model is from the analysis with N_{H} and Γ tied between observations and N_{H} for the inner nebula and pulsar fixed to the best-fit value ($N_{\mathrm{H}} = 13.1 \times 10^{22} \text{ cm}^{-2}$) for the PWN. Lower panels show fit residuals.

$L_{\mathrm{X}} = 5.4 \times 10^{34} \text{ erg s}^{-1} (d/5 \text{ kpc})^2$. For PSR J1813–1749, $\Gamma = 1.2 \pm 0.1$ and $f_{2-10}^{\mathrm{abs}} \approx 1.5 \times 10^{-12} \text{ erg cm}^{-2} \text{ s}^{-1}$, which results in $f_X = 3.1 \times 10^{-12} \text{ erg cm}^{-2} \text{ s}^{-1}$ and $L_{\mathrm{X}} = 9.3 \times 10^{33} \text{ erg s}^{-1} (d/5 \text{ kpc})^2$. The X-ray luminosity relative to spin-down power of PSR J1813–1749 is $L_{\mathrm{X}}/\dot{E} = 1.7 \times 10^{-4}$ (assuming a distance of 5 kpc), and it is $L_{\mathrm{X}}(\mathrm{PWN})/\dot{E} = 9.6 \times 10^{-4}$ for the PWN; these are typical for rotation-

powered pulsars (Becker & Trümper 1997; Becker 2009; Enoto et al. 2019).

We briefly compare our spectral fitting results to those of previous works. Helfand et al. (2007) fit the PWN spectra (ObsID 6685) with absorption $N_{\mathrm{H}} = 9.8_{-0.9}^{+1.2} \times 10^{22} \text{ cm}^{-2}$, $\Gamma = 1.3 \pm 0.3$ (errors are at 90 percent confidence), and $f_{2-10}^{\mathrm{abs}} = 5.6 \times 10^{-12} \text{ erg cm}^{-2} \text{ s}^{-1}$. Spectra of the inner nebula and pulsar are each fit with a PL and fixing N_{H} to that of the PWN. The inner nebula spectral fit yields $\Gamma = 0.4_{-0.7}^{+0.4}$ and $f_{2-10}^{\mathrm{abs}} = 4 \times 10^{-13} \text{ erg cm}^{-2} \text{ s}^{-1}$, while the pulsar spectral fit yields $\Gamma = 1.3 \pm 0.3$ and $f_{2-10}^{\mathrm{abs}} = 1.3 \times 10^{-12} \text{ erg cm}^{-2} \text{ s}^{-1}$. Kuiper & Hermsen (2015) analyse a 98 ks *XMM-Newton* EPIC-pn spectrum taken on 2009 March 27 (ObsID 0552790101) and, with an extraction radius of $15''$ which includes some contribution from the PWN, find a consistent photon index $\Gamma = 1.31 \pm 0.01$ and flux $f_{2-10}^{\mathrm{abs}} = (1.94 \pm 0.11) \times 10^{-12} \text{ erg cm}^{-2} \text{ s}^{-1}$ but somewhat higher absorption $N_{\mathrm{H}} = (11.7 \pm 0.35) \times 10^{22} \text{ cm}^{-2}$. Townsley et al. (2018) fit the 2006 and 2016 *Chandra* spectral data used here and find $N_{\mathrm{H}} = (17 \pm 2) \times 10^{22} \text{ cm}^{-2}$, $\Gamma = 1.6 \pm 0.3$, and absorbed 2–8 keV flux $f_{2-8}^{\mathrm{abs}} = (0.8 - 0.9) \times 10^{-12} \text{ erg cm}^{-2} \text{ s}^{-1}$.

Other than absorption N_{H} , our best-fit model parameter values for the PWN, inner nebula, and pulsar agree with those of Helfand et al. (2007) in their analysis of just the 2006 *Chandra* data, except for a ≈ 20 percent difference in inferred flux of the PWN, and with the parameter values of Kuiper & Hermsen (2015) and Townsley et al. (2018). For N_{H} , our fit to the PWN spectrum using either the 2006, 2016, or combined data yields $N_{\mathrm{H}} \sim (12 - 15) \times 10^{22} \text{ cm}^{-2}$, which is significantly higher than Helfand et al. (2007) find from their fit to the 2006 observation, i.e., $\approx (9 - 11) \times 10^{22} \text{ cm}^{-2}$ [see also Marelli et al. 2011, who find $\approx (5 - 13) \times 10^{22} \text{ cm}^{-2}$]. Note that the Galactic HI column density in the direction of PSR J1813–1749 implies only $N_{\mathrm{H}} = 1.7 \times 10^{22} \text{ cm}^{-2}$ (HI4PI Collaboration et al. 2016). A similarly high absorption, albeit with large uncertainties, is obtained in our fit to the pulsar (or inner nebula) 2006 or 2016 spectrum, which is in agreement with $\sim 17 \times 10^{22} \text{ cm}^{-2}$ from the pulsar spectral fits of Townsley et al. (2018). In addition, fits of *XMM-Newton* data, which cannot fully separate PWN and pulsar emission components, yield a high absorption of $N_{\mathrm{H}} \approx (10 - 13) \times 10^{22} \text{ cm}^{-2}$ (Funk et al. 2007) and $(11 - 12) \times 10^{22} \text{ cm}^{-2}$ (Kuiper & Hermsen 2015). Therefore, a higher value of N_{H} than that found by Helfand et al. (2007) is likely more indicative of the X-ray absorption of the PWN and pulsar (see also discussion of N_{H} and its implication on the distance to PSR J1813–1749 in Halpern et al. 2012).

3 TIMING ANALYSIS OF NICER DATA

We process and filter *NICER* data of PSR J1813–1749 (see Table 1) using HEASoft 6.26.1, NICERDAS 2019-06-19_V006a, and the `psrpipe.py` script from the NICERsoft package². We exclude all events from “hot” detector 34, which gives elevated count rates in some circumstances, and portions of exposure accumulated during passages through the South Atlantic Anomaly. *NICER* experienced a time stamp anomaly which resulted in incorrect time stamps for

² <https://github.com/paulray/NICERsoft>

data taken with MPU1 between 2019 July 8 and 23; we follow the recommended procedure for excluding MPU1 data (for only ObsIDs 2579030201–4) from our analysis³. Using these filtering criteria, we obtain a total of 301,084 events for pulse timing analysis with individual exposure times shown in Table 1 and a total exposure time of 159 ks. We run `barycorr` to transform between Terrestrial Time, used for event time stamps, and Barycentric Dynamical Time (TDB). We adopt the JPL-DE405 solar system ephemeris and absolute sky position measured using the most recent *Chandra* observation (ObsID 17440 from 2016 June 5), i.e., R.A.=18^h13^m35^s.112, decl.=−17°49'57".57 (J2000).

NICER is sensitive to 0.25–12 keV photons. Previous measurements of the 44.7 ms spin period of PSR J1813–1749 are made at 2–10 keV using *Chandra* and *XMM-Newton* with a pulsed fraction \approx 50 percent (Gotthelf & Halpern 2009; Halpern et al. 2012; Kuiper & Hermsen 2015) and at \sim 2–27 keV using *RXTE*, with pulsations being stronger at lower energies (Kuiper & Hermsen 2015). As we show in Section 2.2 and in agreement with previous works, the pulsar spectrum suffers from strong interstellar absorption ($N_{\mathrm{H}} \sim 10^{23} \text{ cm}^{-2}$). Therefore we initially select data in the 1–10 keV range, resulting in 218,624 events. We do not conduct spectral analyses using *NICER* data since the large non-imaging field of view implies an extracted spectrum will primarily be due to that of the PWN and supernova remnant, and spectra from *Chandra* and *XMM-Newton* of these extended sources are presented in other studies (Funk et al. 2007; Helfand et al. 2007).

We perform a blind pulsation search on the merged dataset of all 14 *NICER* observations, using the time differencing technique applied to gamma-ray data in previous works (Atwood et al. 2006; Abdo et al. 2009; Saz Parkinson et al. 2010). We use a time window of 524,288 seconds (Fast Fourier Transform size = 67108864, with resolution of 1.90735×10^{-6} Hz) and scan $\dot{\nu}/\nu$ between 0 and 1.300×10^{-11} Hz in 6494 steps of 2.002×10^{-15} Hz. The best pulsation candidate has a frequency $\nu = 22.35194397$ Hz and $\dot{\nu} = -6.480 \times 10^{-11}$ Hz s $^{-1}$ at MJD 58527.51318287 (mid-point of observations), with a p-value of 8.9×10^{-7} . Recall that Halpern et al. (2012) determine an incoherent timing model with $\nu = 22.3717124$ Hz and $\dot{\nu} = -6.333 \times 10^{-11}$ Hz s $^{-1}$ at MJD 54918.14; this $\dot{\nu}$ leads to a frequency change $\Delta\nu = -0.01975$ Hz by the time of the *NICER* observations and an expected $\nu = 22.35196$ Hz, which closely matches our detection, while a $\ddot{\nu}$ contribution, assuming a braking index $n \equiv \nu\ddot{\nu}/\dot{\nu}^2 = 3$, would only change the $\dot{\nu}$ from Halpern et al. (2012) by 0.3 percent to $\dot{\nu} \approx -6.317 \times 10^{-11}$ Hz s $^{-1}$.

We improve detection significance and refine the timing model using a Markov Chain Monte Carlo (MCMC) refiner in combination with the PINT package⁴ and the *H*-statistic as a measure of significance (de Jager et al. 1989; de Jager & Büsching 2010). Here we ignore the first observation (ObsID 1020440101) because of its short exposure time and because it is too far removed in time (ten months) from the other observations to smoothly connect with the timing model ob-

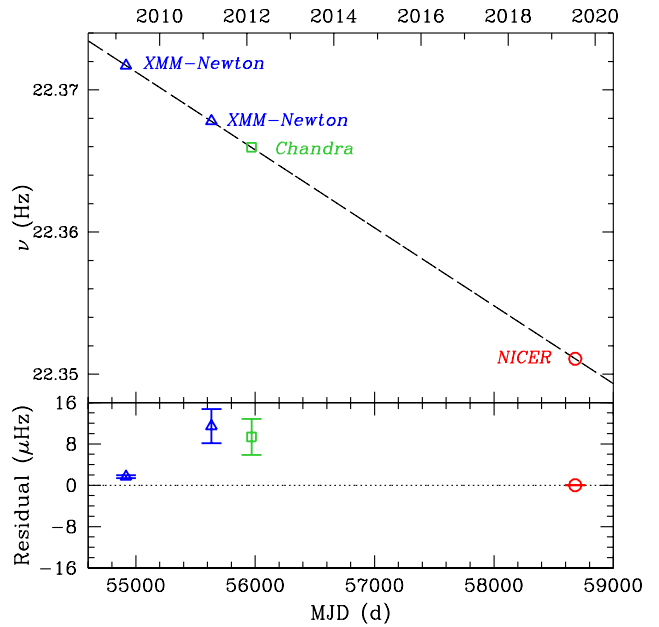


Figure 4. Top: Spin frequency of PSR J1813–1749 as measured using *XMM-Newton* in 2009 and 2011, *Chandra* in 2012, and *NICER* in 2019. Dashed line shows a linear model fit to the spin frequencies, with best-fit slope $\dot{\nu} = -6.3445 \times 10^{-11}$ Hz s $^{-1}$. Bottom: Spin frequency residual after subtracting off the best-fit linear model. Error bars are 1σ uncertainty in measured ν .

tained from these later observations. We add an increasing number of terms in frequency derivative and stop at $\ddot{\nu}$ (see below) since the addition of $\ddot{\nu}$ only yields a marginal *H*-test improvement. We use TEMPO2 (Hobbs et al. 2006) with the `photons` plugin⁵ to assign pulse phases to each event. Then using the `ni_Htest_sortgti.py` script from the NICERsoft package, we determine the optimum energy range to be 3.0–9.2 keV (124,656 events), which yields a maximum significance of 10.1σ ; we note that the choice of lowest energy to include has a large impact on detection significance while the choice of highest energy produces very similar significance levels. The resulting timing model has $\nu = 22.351086 \pm 0.000002$ Hz, $\dot{\nu} = (-6.07 \pm 0.01) \times 10^{-11}$ Hz s $^{-1}$, and $\ddot{\nu} = (-1.0221 \pm 0.0001) \times 10^{-17}$ Hz s $^{-2}$. The large negative value of $\ddot{\nu}$ implies that, not only is $\dot{\nu}$ becoming more negative, but $\dot{\nu}$ changes significantly over the short timespan covered by the timing model, i.e., $|\Delta\dot{\nu}/\dot{\nu}| = 0.55$ in 37.5 days. Such a $\ddot{\nu}$ cannot be the pulsar’s long-term value since it would produce a different $\dot{\nu}$ from that determined about a decade ago. Figure 4 shows the spin frequency of PSR J1813–1749 over the last ten years, i.e., those from 2009–2012 measured by Halpern et al. (2012) and our 2019 narrow windows search result (see below). A simple linear model fit to these ν yields a best-fit spin-down rate of $\dot{\nu} = (-6.3445 \pm 0.0004) \times 10^{-11}$ Hz s $^{-1}$, which is within 3σ of that determined by Halpern et al. (2012), i.e., $\dot{\nu} = (-6.3335 \pm 0.0032) \times 10^{-11}$ Hz s $^{-1}$, and is clearly the long-term spin-down rate of the pulsar. In ad-

³ https://heasarc.gsfc.nasa.gov/docs/nicer/data_analysis/nicer_analysis_tips.html#July2019-MPU1_Timing_Errors

⁴ <https://github.com/nanograv/PINT>

⁵ http://www.physics.mcgill.ca/~aarchiba/photons_plug.html

Table 4. Timing parameters of PSR J1813–1749. Two sets of parameters are provided: The first is from a narrow windows search of only the 2019 *NICER* data (see text); the second is from a linear fit of ν from 2009–2012 and ν from the first set. Number in parentheses is 1σ error in last digit.

Parameter	Value
R.A. (J2000)	18 ^h 13 ^m 35 ^s .112
Decl. (J2000)	-17°49'57".57
Position epoch (MJD)	57544
Timing reference epoch (MJD)	58681.04405092593
Spin frequency ν (Hz)	22.351083818(17)
2019 June–2019 August	
Timespan of model (MJD)	58662.3–58699.8
Frequency derivative $\dot{\nu}$ (Hz s ⁻¹)	-6.4283(33) × 10 ⁻¹¹
2009 March–2019 August	
Timespan of model (MJD)	54918.14–58699.8
Frequency derivative $\dot{\nu}$ (Hz s ⁻¹)	-6.34450(44) × 10 ⁻¹¹

dition to the blind searches described above, we perform a search in narrow windows around the expected ν and $\dot{\nu}$ (i.e., $\nu = [22.35108 \text{ Hz}, 22.35108995 \text{ Hz}]$ with steps of $5 \times 10^{-8} \text{ Hz}$ and $\dot{\nu} = [-7 \times 10^{-11} \text{ Hz s}^{-1}, -6 \times 10^{-11} \text{ Hz s}^{-1}]$ in steps of $1 \times 10^{-13} \text{ Hz s}^{-1}$) and assuming $\ddot{\nu} = 0$. Search results (with H -test value of 72) are presented in Table 4, including a $\dot{\nu} = (-6.428 \pm 0.003) \times 10^{-11} \text{ Hz s}^{-1}$, which differs but is much closer to the long-term value.

To investigate possible changes in the timing parameters within the *NICER* dataset, we break the dataset into three segments, i.e., ObsIDs 2579030101–3 (2019 June 28–30) for 52 ks of total exposure, ObsIDs 2579030201–4 (July 10–13) for 50 ks, and ObsIDs 2579030301–6 (July 30–August 4) for 49 ks. The first *NICER* observation of 6 ks exposure time (ObsID 1020440101) is dropped since it is not long enough to yield an independent detection on its own. A blind search is run on each segment independently, with the same search parameters as given above. A clear detection is made only in the third segment, and the best pulsation candidate has $\nu = 22.35099411 \text{ Hz}$ and $\dot{\nu} = -6.217 \times 10^{-11} \text{ Hz s}^{-1}$, which are consistent with results from the merged dataset search, with a p-value of 5.62×10^{-5} . Meanwhile, performing a search of each segment in a narrow window, with steps in ν of $1 \times 10^{-7} \text{ Hz}$ but using a fixed $\dot{\nu} = -6.428 \times 10^{-11} \text{ Hz s}^{-1}$, yields a detection in all three segments (H -test values > 30). There is also evidence from the structure of the significance peaks in ν in the third segment that a glitch of magnitude $\Delta\nu \approx 3 \mu\text{Hz}$ occurred on MJD 58698, but data limitations prevent a more definitive conclusion.

In summary, Table 4 presents the final parameters of two timing models we derived above. The first is based on only the narrow windows search of the 37 d span in 2019 of *NICER* data. The second is based on the linear fit to the long-term ten-year spin frequency evolution starting from 2009 to our 2019 measurement using *NICER* and shown in Figure 4. The main distinction between the two is $\dot{\nu} = -6.428 \times 10^{-11} \text{ Hz s}^{-1}$ in the former and $\dot{\nu} = -6.3445 \times 10^{-11} \text{ Hz s}^{-1}$ in the latter. We also show in Figure 5 the 3–9.2 keV pulse profile using *NICER* data and the *NICER*-only timing model; because *NICER* cannot spatially resolve PWN and supernova remnant contributions to the unpulsed component of the pulse profile, an estimate of the

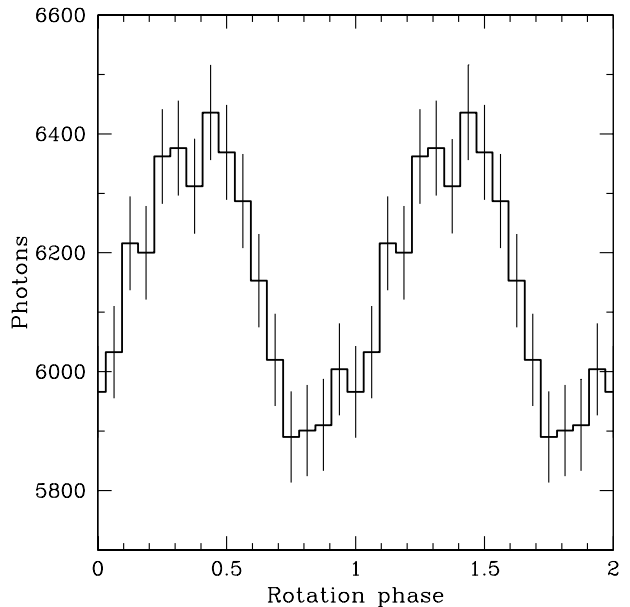


Figure 5. Pulse profile (3–9.2 keV) of PSR J1813–1749 using the 2019-only timing model given in Table 4. Two rotation cycles are shown, with 16 bins per cycle. Error bars are 1σ .

pulsed fraction would be unreliable. There are several possible explanations for the differing spin-down values, such as the pulsar's timing behavior is affected by timing noise, glitches, and/or mode switching. First, young pulsars, such as PSR J1813–1749, tend to exhibit timing noise (Hobbs et al. 2010; Shannon & Cordes 2010; Espinoza et al. 2017). For example, PSR J1124–5916 in the supernova remnant G292.0+1.8 has comparable spin properties but is noisy; it also has a low negative braking index and glitched at least once (Ray et al. 2011). As for glitches, PSR J1813–1749 could glitch at a rate as high as once every ≈ 200 d, based on its spin-down rate $\dot{\nu}$ (Haskell et al. 2012). In this case, there is a ≈ 15 percent probability one glitch occurred during the *NICER* observations if glitch occurrence follows Poisson statistics, and we indeed have tentative evidence for the occurrence of such a glitch. However, Fuentes et al. (2017, 2019) find that, while glitch activity correlates with spin-down rate for $|\dot{\nu}| < 10^{-10.5} \text{ Hz s}^{-1}$ and is highest at the top of this range, some pulsars with even greater $|\dot{\nu}|$ show lower glitch activity. Thus PSR J1813–1749 could have a relatively low rate of glitches since it has a $|\dot{\nu}| = 10^{-10.2} \text{ Hz s}^{-1}$, but this is far from certain. Lastly, some pulsars switch between radio emission states, such that their spin-down rate can be up to 50 percent higher when in an active state (Kramer et al. 2006; Lyne et al. 2010; Hermsen et al. 2017). In the case of PSR J1813–1749, the best-fit long-term spin-down rate differs from that of the timing model by only 1 percent. Dzib et al. (2018) indicate pulsed radio emission may have been detected but only at high frequencies due to extreme scattering. An interesting comparison could potentially be made between PSR J1813–1749 and the third highest \dot{E} pulsar, PSR B0540–69, which glitches and has a similar age (~ 1000 yr) and spin rate (= 19.7 Hz) and $\dot{\nu}$ and $\ddot{\nu}$ that

changed from -1.87×10^{-10} Hz s $^{-1}$ to -2.53×10^{-10} Hz s $^{-1}$ and 3.7×10^{-21} Hz s $^{-2}$ to 0.1×10^{-21} Hz s $^{-2}$, respectively, due possibly to a switch between radio emission states (Ferdman et al. 2015; Marshall et al. 2015, 2016). More extensive X-ray monitoring and continued searches in radio may be able to answer this issue.

4 DISCUSSIONS

In this work, we analyze *Chandra* and *NICER* observations of the highly energetic rotation-powered pulsar PSR J1813–1749. The ten years between *Chandra* observations allow us to measure a pulsar proper motion $\mu_{\text{RA.}} = -0''.067$ yr $^{-1}$ and $\mu_{\text{decl.}} = -0''.014$ yr $^{-1}$, which implies a transverse velocity $v_{\perp} = 1600$ km s $^{-1}$ ($d/5$ kpc); note the distance is uncertain, with a range of 3–5 kpc (Messineo et al. 2011; Halpern et al. 2012). *Chandra* spectra of the pulsar and its PWN can each be well-fit by an absorbed power law model and reveal no evidence of significant changes in flux and model parameters between observations. However, we find that the X-ray absorption ($N_{\text{H}} = 13.1 \times 10^{22}$ cm $^{-2}$) is higher than that found in early studies but in agreement with more recent works. We detect pulsations at the 44.7 ms spin period of PSR J1813–1749 using recent *NICER* data. We find that the spin-down rate determined over the past decade differs from that measured over a month with the timing model.

The spin period of PSR J1813–1749 has only been previously measured using *XMM-Newton* in 2009 and 2011 and *Chandra* in 2012 and not found in radio or using *Fermi* (Halpern et al. 2012; Kuiper & Hermsen 2015). The pulsar is a target of interest for gravitational wave (GW) searches. These searches are beginning to achieve meaningful constraints on possible energy loss due to GW emission in the case of PSR J1813–1749 (Abbott et al. 2017, 2019a). The most sensitive searches that can be conducted are those that have contemporaneous electromagnetic timing models (Abbott et al. 2019b). If such a timing model had been available for PSR J1813–1749, an improvement of ~ 5 on upper limits to GW strain and ~ 25 to GW energy would have been possible over those obtained in the less sensitive search by Abbott et al. (2019a). Efforts are underway to search the latest, most sensitive GW data from the third observing run (O3), which collected data from 2019 April 1 to 2020 March 27. The contemporaneous timing model provided here using *NICER* data will enable improved limits on GW emission from this highly energetic pulsar.

ACKNOWLEDGEMENTS

The authors thank the anonymous referee for comments which led to improvements in the manuscript. WCGH thanks D.L. Kaplan and G.G. Pavlov for helpful comments on astrometry analysis, P.S. Ray for advice on timing analysis, and W.A. Majid for comments on an early draft. WCGH appreciates use of computer facilities at the Kavli Institute for Particle Astrophysics and Cosmology. WCGH acknowledges support through grant 80NSSC19K1444 from NASA. SG acknowledges support of CNES. MB is partially supported by Polish NCN grant no. 2017/26/M/ST9/00978.

CME acknowledges funding from ANID grant FONDECYT/Regular 1171421. CM is supported by an appointment to the NASA Postdoctoral Program at Marshall Space Flight Center, which is administered by Universities Space Research Association under contract with NASA.

DATA AVAILABILITY

The data underlying this article will be shared on reasonable request to the corresponding author.

REFERENCES

- Abbott et al. 2017, *Phys. Rev. D*, **96**, 122006
- Abbott et al. 2019a, *Phys. Rev. D*, **99**, 122002
- Abbott et al. 2019b, *ApJ*, **879**, 10
- Abdo A. A., et al., 2009, *Science*, **325**, 840
- Aharonian F., et al., 2005, *Science*, **307**, 1938
- Arnaud K. A., 1996, in Jacoby G. H., Barnes J., eds, Astronomical Society of the Pacific Conference Series Vol. 101, Astronomical Data Analysis Software and Systems V. p. 17
- Atwood W. B., Ziegler M., Johnson R. P., Baughman B. M., 2006, *ApJ*, **652**, L49
- Becker W., 2009, X-Ray Emission from Pulsars and Neutron Stars. p. 91, doi:10.1007/978-3-540-76965-1_6
- Becker W., Trümper J., 1997, *A&A*, **326**, 682
- Brogan C. L., Gaensler B. M., Gelfand J. D., Lazendic J. S., Lazio T. J. W., Kassim N. E., McClure-Griffiths N. M., 2005, *ApJ*, **629**, L105
- Dang S. J., et al., 2020, *ApJ*, **896**, 17
- Deller A. T., et al., 2019, *ApJ*, **875**, 100
- Dzib S., Loinard L., Rodríguez L. F., 2010, *Rev. Mex. Astron. Astrofis.*, **46**, 153
- Dzib S. A., Rodríguez L. F., Karuppusamy R., Loinard L., Medina S.-N. X., 2018, *ApJ*, **866**, 100
- Enoto T., Kisaka S., Shibata S., 2019, *Reports on Progress in Physics*, **82**, 106901
- Espinosa C. M., Lyne A. G., Stappers B. W., 2017, *MNRAS*, **466**, 147
- Ferdman R. D., Archibald R. F., Kaspi V. M., 2015, *ApJ*, **812**, 95
- Fruscione A., et al., 2006, in Society of Photo-Optical Instrumentation Engineers (SPIE) Conference Series. p. 62701V, doi:10.1117/12.671760
- Fuentes J. R., Espinosa C. M., Reisenegger A., Shaw B., Stappers B. W., Lyne A. G., 2017, *A&A*, **608**, A131
- Fuentes J. R., Espinosa C. M., Reisenegger A., 2019, *A&A*, **630**, A115
- Funk S., et al., 2007, *A&A*, **470**, 249
- Gotthelf E. V., Halpern J. P., 2009, *ApJ*, **700**, L158
- HI4PI Collaboration et al., 2016, *A&A*, **594**, A116
- Halpern J. P., Gotthelf E. V., Camilo F., 2012, *ApJ*, **753**, L14
- Haskell B., Pizzochero P. M., Sidery T., 2012, *MNRAS*, **420**, 658
- Helfand D. J., Gotthelf E. V., Halpern J. P., Camilo F., Semler D. R., Becker R. H., White R. L., 2007, *ApJ*, **665**, 1297
- Hermsen W., et al., 2017, *MNRAS*, **466**, 1688
- Hobbs G. B., Edwards R. T., Manchester R. N., 2006, *MNRAS*, **369**, 655
- Hobbs G., Lyne A. G., Kramer M., 2010, *MNRAS*, **402**, 1027
- Kargaltsev O., Pavlov G. G., Klingler N., Rangelov B., 2017, *Journal of Plasma Physics*, **83**, 635830501
- Kramer M., Lyne A. G., O'Brien J. T., Jordan C. A., Lorimer D. R., 2006, *Science*, **312**, 549
- Kuiper L., Hermsen W., 2015, *MNRAS*, **449**, 3827
- Lyne A., Hobbs G., Kramer M., Stairs I., Stappers B., 2010, *Science*, **329**, 408

- Manchester R. N., Hobbs G. B., Teoh A., Hobbs M., 2005, *AJ*, **129**, 1993
Marelli M., De Luca A., Caraveo P. A., 2011, *ApJ*, **733**, 82
Marshall F. E., Guillemot L., Harding A. K., Martin P., Smith D. A., 2015, *ApJ*, **807**, L27
Marshall F. E., Guillemot L., Harding A. K., Martin P., Smith D. A., 2016, *ApJ*, **827**, L39
Messineo M., Davies B., Figer D. F., Kudritzki R. P., Valenti E., Trombley C., Najarro F., Rich R. M., 2011, *ApJ*, **733**, 41
Ray P. S., et al., 2011, *ApJS*, **194**, 17
Sax Parkinson P. M., et al., 2010, *ApJ*, **725**, 571
Shannon R. M., Cordes J. M., 2010, *ApJ*, **725**, 1607
Townsley L. K., Broos P. S., Garmire G. P., Anderson G. E., Feigelson E. D., Naylor T., Povich M. S., 2018, *ApJS*, **235**, 43
Ubertini P., et al., 2005, *ApJ*, **629**, L109
Verner D. A., Ferland G. J., Korista K. T., Yakovlev D. G., 1996, *ApJ*, **465**, 487
Wilms J., Allen A., McCray R., 2000, *ApJ*, **542**, 914
de Jager O. C., Büsching I., 2010, *A&A*, **517**, L9
de Jager O. C., Raubenheimer B. C., Swanepoel J. W. H., 1989, *A&A*, **221**, 180

This paper has been typeset from a *TeX/L^AT_EX* file prepared by the author.